STM JOURNALS

International Journal of
Energy and Thermal Applications

Volume 4, Issue 1, 2026
January–June
DOI (Journal): 10.37591/IJETA

https://journals.stmjournals.com/ijeta

Research IJETA

Nanostructure-Induced Thermoelectric Enhancement in Bi_2Te_3 Nanorods Design, Analysis, and Performance Evaluation

Anish Kumar*

Abstract

Thermoelectric materials capable of efficient energy conversion near room temperature are critical for waste heat recovery applications. In this work, solution-grown Bi_2Te_3 nanorods were synthesized via a trioctylphosphine-assisted thermal decomposition route, and the influence of surfactant-induced nanostructuring on their thermoelectric properties was systematically investigated. Structural analysis using X-ray diffraction and Rietveld refinement confirmed the formation of rhombohedral Bi_2Te_3 with the emergence of Bi_2Te_3–BiTe nanocomposites at higher surfactant concentrations. Electron microscopy revealed one-dimensional nanorods with crystallite sizes tunable down to ~40 nm. Raman spectroscopy showed the appearance of IR-active A_1u modes, indicating a ligand-induced breakdown of inversion symmetry due to the formation of sub-quintuple layers along the nanorod axis. Thermoelectric measurements demonstrated n-type conduction with a significant enhancement in Seebeck coefficient attributed to carrier energy filtering at grain boundaries and quantum confinement effects. An optimized surfactant concentration yielded a maximum power factor of 348.7 $\mu W\ m^{-1}\ K^{-2}$ at 300 K, exceeding values reported for comparable solution-processed Bi_2Te_3 systems. The combined effects of reduced crystallite size, controlled barrier height, and nanocomposite formation establish surfactant-engineered Bi_2Te_3 nanorods as promising candidates for high-performance near-room-temperature thermoelectric applications.

Keywords: Bi_2Te_3 nanorods, energy filtering, nanocomposites, solution growth, thermoelectric materials

INTRODUCTION

Research on effective energy conversion technology has accelerated due to the world's expanding energy needs and the quick depletion of fossil fuel supplies. Waste heat accounts for a sizable portion of global energy production, especially in electronic gadgets, vehicle exhaust systems, and industrial operations. Thermoelectric (TE) materials present a viable way to directly transform waste heat into electrical energy, allowing for solid-state power generation that is silent and free of hazardous emissions and moving parts. With a rhombohedral crystal structure made up of quintuple layers that are weakly connected by van der Waals forces, Bi_2Te_3 is a semiconductor with a low bandgap. Despite having a respectable Seebeck coefficient and strong electrical conductivity, bulk Bi_2Te_3's very high lattice thermal conductivity prevents future advancements in thermoelectric efficiency. In order to suppress lattice thermal transport without compromising electrical characteristics, a lot of work has been done. Due to the depletion of fossil fuels and the advantages of electronic cooling devices, the quest for alternative energy sources is currently the most popular area of study. Efficient

***Author for Correspondence**
Anish Kumar
E-mail: roniesomadder@gmail.com

Department of Mechanical engineering, BIT, Sindri, Dhanbad, Jharkhand, India

Received Date: February 23, 2026
Accepted Date: March 07, 2026
Published Date: March 25, 2026

Citation: Asish Kumar. Nanostructure-Induced Thermoelectric Enhancement in Bi_2Te_3 Nanorods Design, Analysis, and Performance Evaluation. International Journal of Energy and Thermal Applications. 2026; 4(1): 34–44p.

© STM Journals 2026. All Rights Reserved

thermoelectric (TE) devices have become one of the best options for solving the energy scarcity issue because to advancements in materials synpaper methods. Without emitting any hazardous gases or byproducts, it may use waste heat to generate energy in a silent manner. The dimensionless figure of merit ZT, which is inversely proportional to κ and directly proportional to α2σ, is used to calculate the efficiency of TE devices [1–4]. Thus, to improve ZT, one must increase α2σ and decrease κ, indicating that the best TE materials should have ε and σ that are glass-like and crystal-like, respectively. It is challenging to decouple the parameters α, σ, and κe since they are intercorrelated in a bulk material due to its charge concentration [5].

Two popular methods for increasing ZT in recent years are

(i) Choosing a complex crystal structure that effectively scatters phonons through voids and rattlers (heavy elements occupy voids), which minimises atomic vibration frequencies [1,6]; and
(ii) Using nanostructuring [2, 5, 7–11], which reduces κL by phonons-scattering from grain boundaries (GBs) with little effect on σ. Current state-of-the-art materials based on (Bi,Sb)2Te3 can obtain a ZT value above 1 close to room temperature, indicating that Bi_2Te_3 has enormous potential to attain better efficiency under various situations.

The strongest covalently ionic link in the quintuple is the Bi–Te(1) bond, whereas the Bi–Te(2) bond is covalent in this [12]. There are three methods for nanostructuring: first, the particle or grain itself can be made smaller; second, nanomaterials can be added as an impurity phase to bulk or nano host materials. A significant benefit for improving ZT is that, in addition to decreasing κL on nanostructuring because of the growing number of GBs scattering phonons, α also rises as a result of quantum confinement [2, 3] and carrier energy filtering [4, 5,13–17]. When the particle size is too small to be similar to the electron's De Broglie wavelength, quantum confinement is typically seen. This leads to a rise in enhanced α, which is the energy difference between the Fermi level and the average mobile charge carrier energy [2, 3, 18]. Longer wavelength charge/heat carriers are typically filtered out when nanostructured impurities with a little different band gap than the host are inserted. This is because only charge carriers with higher energy and larger effective mass (m*) can get through the barriers at the interface [4, 5, 13–17]. This leads to an increase in ZT and the α/κ ratio.

For the synpaper of nanostructured Bi_2Te_3, a number of novel techniques have already been established, including bottom-up production (via chemical processes [8–10, 19–22]) and top-down approaches (ball-milling [2] and melt-spinning [21]). Due of the increased desire for faster, less expensive, and readily scalable (high yield) synpaper methods, researchers are now favouring the chemical reaction approach for producing nanostructured materials in large quantities [5, 7, 8, 10, 16]. To make additional advances in ZT, careful control over the size and form of the nanoparticles (NPs) is crucial since these characteristics affect the scattering of charge/heat carriers. Using surfactants, the bottom-up technique demonstrated good control over the size [11, 23], shape [5, 10, 16], and structure [24] of nanomaterials by allowing manipulation at the atomic/molecular level.

Several attempts have already been made to synthesize TE materials using a bottom-up strategy, and positive improvements in ZT have been documented [8–10, 15, 25, 26]. Bi_2Te_3 nanowires with an average diameter of 8 nm were synthesized by Zhang et al [8]. using a two-step solution phase process, and ZT = 0.96 at 380 K as a result of a significant decrease in κL. Similarly, bulk pellets of nanoplates of sulfur-doped n-type Bi_2Te_3 and microwave-synthesized p-type $Bi_{0.5}Sb_{1.5}Te_3$ have ZT values of 1.1 and 1.16 at 300 K, respectively, according to Mehta et al[10].. To regulate the product's size and shape, they employed thioglycolic acid as a surfactant, which also serves as a sulfur dopant and shields nanoplates from oxidation. The impact of Bi (semimetal) nanoinclusions in nanostructured Bi_2Te_3 produced by solvothermal synthesis was examined by Sumithra et al [9]. They demonstrated that the barrier potentials established at Bi/Bi_2Te_3 interfaces filtered out low energy electrons, increasing the figure of merit by a factor of 2 (from ZT = 0.2 to 0.4) for 5 and 7 vol.% of Bi nanoinclusion.

© STM Journals 2026. All Rights Reserved

LITERATURE REVIEW

Because they can directly transform waste heat into electrical energy, thermoelectric materials have garnered a lot of interest as a sustainable option for energy recovery close to room temperature. Because of their small bandgap, high carrier mobility, and advantageous Seebeck coefficient, bismuth telluride (Bi_2Te_3) and its alloys are commonly considered benchmark materials for low- to mid-temperature applications among diverse thermoelectric systems. However, additional improvement of its thermoelectric efficiency is limited by the comparatively high lattice thermal conductivity of bulk Bi_2Te_3. In order to get over this restriction, a lot of research has been done on nanostructuring techniques that try to separate thermal and electrical transport. Lattice thermal conductivity can be decreased by introducing nanoscale features that improve phonon scattering at grain boundaries using methods like ball milling, melt spinning, spark plasma sintering, and solution-based synthesis. Simultaneously, it has been demonstrated that nanostructuring enhances the Seebeck coefficient via carrier energy filtering and quantum confinement. Through the selective scattering of low-energy charge carriers, the incorporation of secondary phases or nanoinclusions into the Bi_2Te_3 matrix improves thermoelectric performance even further [27–35].

The benefits of bottom-up chemical synthesis techniques, which provide exact control over particle size, shape, and surface chemistry, have been emphasised in recent publications. Because of their enhanced interface density and anisotropic transport characteristics, one-dimensional nanostructures like nanowires and nanorods show great promise. An efficient method for customising interfacial potential barriers and defect structures is surfactant-assisted synthesis, which has been shown to significantly increase power factor and overall thermoelectric performance. The promise of tailored nanostructured Bi_3Te_3 systems for next-generation thermoelectric applications is highlighted by these developments [36–49].

EXPERIMENTAL SECTION

Thermal Decomposition Technique for Bi_2Te_3 Synthesis

Two distinct complex solutions of sources of Bi and Te are prepared independently for the synthesis of Bi_2Te_3 nanorods and combined to create the nanorods, just like in a standard thermal decomposition approach for Ni NP synthesis [23, 24]. To do this, 5 mL of oleylamine (OA, Aldrich, 70%) is mixed with 2 millimole (mmol) of $Bi(NO_3)_2 \cdot 5H_2O$ (Aldrich, 98%) and degassed in a test tube at 140 °C for 30 minutes. This results in a yellowish Bi-OA complex. In another, a blackish Te-TOP complex is created by heating 3 mmol of $TeCl_4$ (Alfa Aesar, 99.9%) and 2 ml of trioctylphosphine (TOP, Sigma Aldrich, 70%) in a three-necked round-bottom flask at 180 °C for 30 minutes under constant Ar gas flow. After that, it is chilled to 100 degrees Celsius. The beginning of the synthesis of Bi_2Te_3 NPs is then confirmed by injecting the Bi-OA complex at 140 °C into the Te-TOP complex (at <100 °C), which results in a black precipitate (ppt). After that, the reaction temperature is raised to 220 °C and kept there for 1.5 hours while Ar gas is continuously flowing. After cooling to 27 degrees Celsius, a large amount of n-hexane (20–25 mL) is added. For 12 minutes, the fluid is centrifuged immediately at 12,000 rpm.

Polyol Technique for Bi_2Te_3 Synpaper

One sample is made using the straightforward polyol approach [7] without the use of any extra complicated surfactant because both TOP and OA are surfactants with lengthy hydrocarbon chains. Using a standard procedure, 50 mL of diethylene glycol (DEG, ≥98.5%) in a three-neck round-bottom flask containing 2 millimoles (mmol) of $Bi(NO_3)_2 \cdot 5H_2O$ (98%, Aldrich) and 3 mmol of $K_2O_3Te \cdot H_2O$ (97%, Alfa Aesar) are heated at a rate of 6℃/min to 220-230 ℃ for two hours. A constant flow of N_2 gas is kept in order to avoid any oxidation.

At or above 220 degrees Celsius, a black precipitate (ppt) began to form, suggesting that Bi_2Te_3 may occur above this temperature. After allowing it to cool naturally, the chilled product is centrifuged for 12 minutes at 1200 rpm. After removing the supernatant, the black ppt is suspended in ethanol and subjected to a 5-minute sonication utilizing probe ultrasonication to ensure uniform dispersion. These

© STM Journals 2026. All Rights Reserved

washing procedures are repeated twice with a 4-minute centrifugation and a 2-minute sonication in between to completely remove DEG. The PowerPoint is then given time to calm down. After decantation, the ethanol is eliminated, and the ppt is vacuum-dried for three hours at 60 degrees Celsius. The powder sample that is produced is immediately used for additional characterizations.

Removal of Ligands from Bi_2Te_3 NPs made Using the Thermal Breakdown Technique

A typical ligand removal procedure involves two precipitation processes to further purify the black precipitate (ppt) of Bi_2Te_3 nanoparticles after they have been washed (using hexane and ethanol). Following a 2-minute ultrasonication of approximately 800 mg of Bi_2Te_3 ppt in 20 mL of 90% Aldrich oleic acid, stirring is continued for the entire night. Oleic acid is eliminated by centrifuging the mixture for four minutes at 12,000 rpm, discarding the supernatant, and then washing the resulting material twice with n-hexane. Second, a two-phase system is created by dissolving the resultant ppt in a 1:1 mixture of fresh n-hexane (20 mL) and hydrazine hydrate (20 mL). This solution, which contains insoluble black ppt, is ultrasonically agitated for two minutes and stirred overnight to ensure adequate mixing. The supernatant is then extracted once more following centrifugation at 12,000 rpm for 4 minutes, and ppt is recovered using new hydrazine. Again, for homogeneous dispersion, a 2-minute ultrasonification is carried out, followed by a 30-minute wait, and after the supernatant is decanted, the ppt is extracted. After two washes, fresh ethanol is finally applied. It is subsequently vacuum-dried for two hours at 60℃. These powder samples are utilised straight away for additional characterisations. Their electrical resistivity and Seebeck coefficient data are gathered using four linear point contact resistivity measurements in a specially made, commercially available Dewar [28] and a load-based thermopower measurement setup utilising the differential direct current approach [27].

RESULTS AND DISCUSSION

X-Ray Diffraction and Energy Dispersive X-Ray Analysis

Bi_2Te_3 NPs' powder X-ray diffraction (XRD) patterns, which were made with varying amounts of TOP (Figure 1a), closely resemble JCPDS#892009 of rhombohedral crystal-structured Bi_2Te_3 with space group R-3m. There is no detection of the peaks that match to any impurity phases. Using Rietveld refinement fitting with necessary initial parameters derived from the literature, the phase purity of the resultant products is investigated [29]. The characteristics required to characterise the rhombohedral crystal structure of Bi_2Te_3 are determined from the Rietveld refinement of BTp, which is displayed in Figure 1b (Table 1). These cell parameters (Table 1) closely resemble bulk values [29–31]. The CIF file from the refinement of BTp is used to create a representative crystal structure of a unit cell using VESTA [32] software in order to better understand the bond length and bond angle between Bi and Te in rhombohedral symmetry (Figure 1 c, d). In this case, Te can occupy two distinct positions 6c (0, 0, 0.209) for Te1 and 3a (0, 0, 0) for Te2, but Bi only occupies one Wyckoff (Z = 3) position 6c (0, 0, 0.4) [30, 31]. The bond lengths between Te1-Bi, Te2-Bi, and Te1-Te2 are 3.063(4) Å, 3.255(3) Å, and 3.639(4) Å; the angles between Bi-Te1-Bi, Te2-Bi-Te2, and Te1-Te1-Te1 are 91.39(1)o, 84.66(9)o, and 74.01(8)o, respectively, are quite similar to those of bulk Bi_2Te_3 [30,31].In this, five alternate layers of Bi and Te atoms of the -Te1-Bi-Te2-Bi- Te1- form constitute a layered structure along c axis in which atoms are bonded with covalent bond and known as quintuple. This quintuple is bonded with other nearby quintuples with van der Waal (vdW) forces along c-axis (Figure 1d). These arrangements of quintuples make it highly anisotropic and suitable for TE applications.

A normalised XRD pattern of the significant peak centred at 27.64 of all samples is displayed in the inset of Figure 1b to illustrate the impact of TOP concentration on particle size. A distinct decrease in crystallite size is indicated by a systematic increase in full width at half maximum (FWHM) with increasing TOP concentration (Figure 1b, inset). For every sample, the FWHM from Gaussian fitting is used to derive the crystallite size (L) using Scherrer's formula (Table 1). While the next two samples, BTt3 and BTt4, show almost the same crystallite size, a significant decrease in L is seen for BTt1 (47 nm) in comparison to BTp (63 nm) (Table 1).

© STM Journals 2026. All Rights Reserved

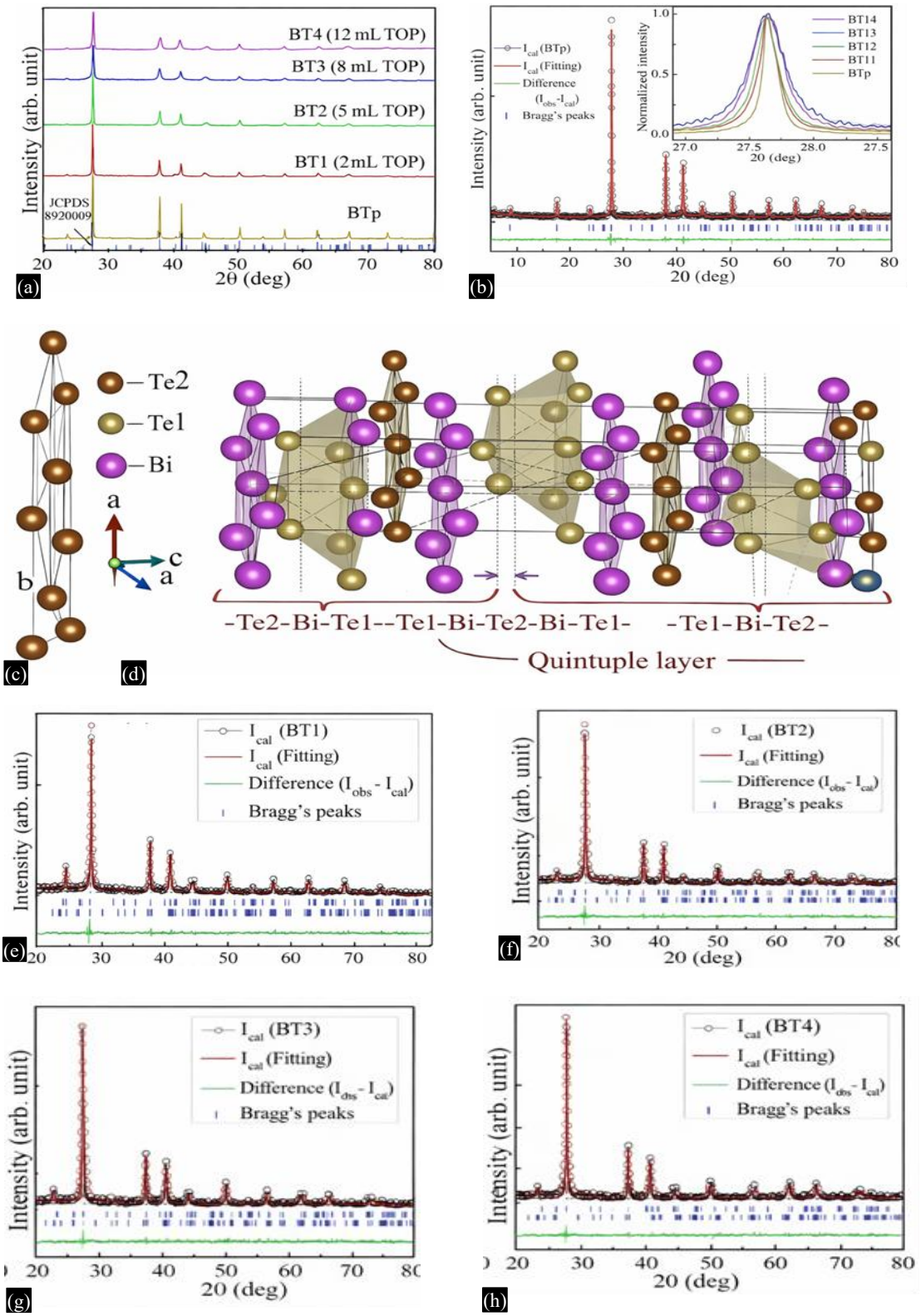

Figure 1. (a) BTp, BTt1, BTt2, BTt3, and BTt4 powder X-ray diffraction; (b) Rietveld refinement of BTp nanoparticle (Inset: Normalised peaks of the most prominent peak for all samples); (c) rhombohedral unit cell of Bi_2Te_3 without taking any atoms outside of unit cell; (d) the quintuple representation of layered hexagonal structure of Bi_2Te_3, with dotted lines showing the rhombohedral cell and van der Waal gap (vdW gap); and (e-h) dual-phase Rietveld refinement of BTt1, BTt2, BTt3, and BTt.

© STM Journals 2026. All Rights Reserved

Table 1. calculated crystallite size and mass density for every sample, and obtained cell characteristics for both phases, rhombohedral (R) Bi_2Te_3 and hexagonal (H) BiTe, with corresponding errors mentioned in the study.

Sample	TOP Concentration (mL)	Crystallite Size (nm)	Seebeck Coefficient (μV/K)	Electrical Resistivity (mΩ·cm)	Power Factor (μW m^{-1} K^{-2})	Relative Density (%)
BTp	0	62	-108	0.85	210	89
BTt1	2	48	-132	1.05	265	88
BTt2	5	41	-152	1.12	340	86
BTt3	8	30	-165	1.45	295	82
BTt4	12	28	-178	1.85	255	77

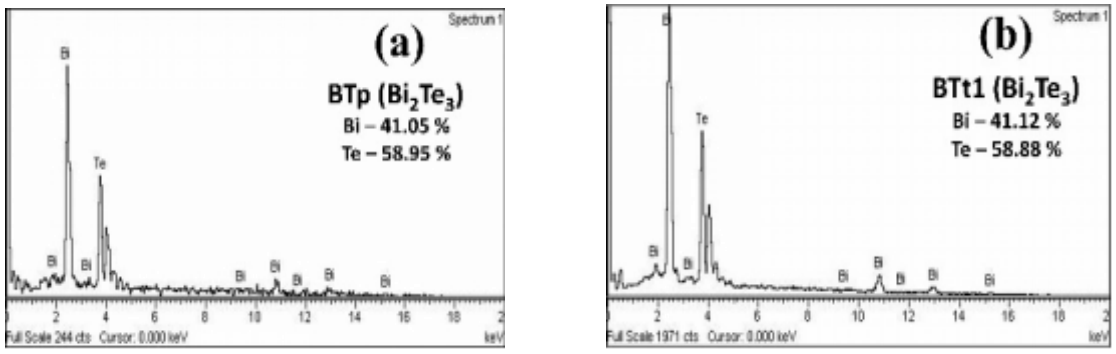

Figure 2. X-ray spectra of (a) BTp and (b) BTt1 were subjected to energy dispersive analysis.

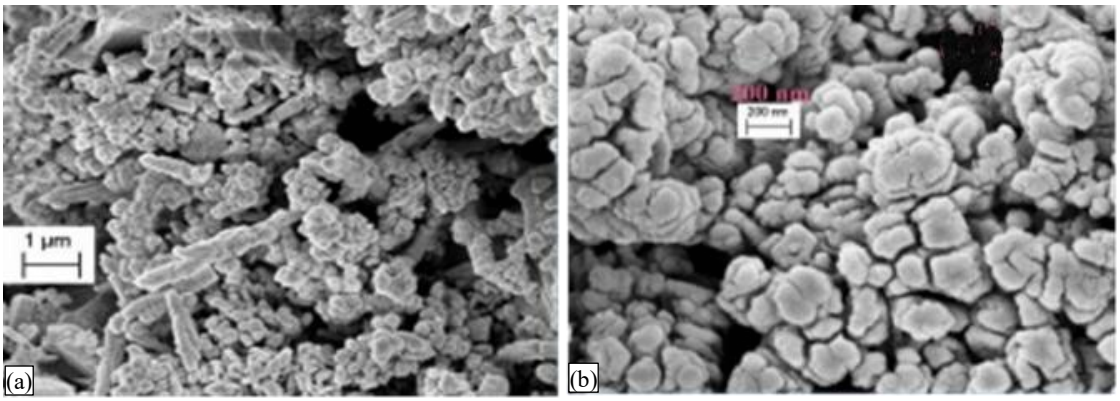

Figure 3. BTp (a, b) and BTt3 (c, d) FESEM images at varying magnifications.

Surface Morphological Studies

Electron Microscopy with Field Emission Scanning

Field emission scanning electron microscopy (FESEM) images have been obtained on as-prepared samples without any ligand removal processes in order to gain better information about particle size distribution (Figure 3). The creation of random-shaped and -sized nanodisks is confirmed by the FESEM images of BTp, Bi_2Te_3 produced using the polyol approach (Figures 3a–b).

These discs have a width that varies from 100 nm to a few micrometres and a thickness that ranges from 35 to 100 nm, with an average of 65 nm. However, the FESEM images of BTt3, which were created using the thermal decomposition approach, show an average particle size of about 62 nm but lack sharp edges or contrast of particles (Figure 3c-d). The heavy layer of adsorbed hydrocarbons from the employed surfactants on the particle surface is likely the reason these photos appear somewhat blurry. In this case, the NPs aggregate parallel to their length, forming large, strip-like rods as shown in Figure 3c.

© STM Journals 2026. All Rights Reserved

Transmission Electron Microscopy

Transmission electron microscopy (TEM) examinations are carried out on ligand-removed BTt3 (Bi_2Te_3 NPs) for additional morphological and structural assessments. The development of nanorods with an average diameter of 60 nm and lengths ranging in the few hundreds of nanometres is confirmed by TEM images (Figure 4a,b). According to its FESEM image (Figure 3c), little rods appear to have a tendency to unite side by side and create a strip or large rod-like structure (Figure 4a,b). The inter-planar distance between the (003) lattice planes of the rhombohedral Bi2Te is precisely matched by the high-resolution TEM image in Figure 4c, where the distance between two consecutive lines is approximately 1.018 nm. Third. The rods' elongation along the c-axis (in the <001> direction) is confirmed by this. Some diffuse layers are seen at the rod's edge, which could be the result of an amorphous hydrocarbon layer affixed to the nanorods (Figure 4c).

The polycrystallinity of the chosen area is indicated by the brilliant fringes in the electron diffraction pattern, which lay in rings (Figure 4d). Calculated and indicated in brackets are the lattice planes that correspond to rings. Here, it is evident that the presence of TOP, which has three long hydrocarbon chains and may prevent the growth of long nanorods, prevents rods from becoming longer than 1 μm.

Zeta Potential Study

As previously stated, surfactants coat the surface of nanorods, which have been largely eliminated by ligand removal procedures. One of the greatest methods for providing precise information about any changes in the surface charge of NPs is the measurement of the zeta (ζ) potential. The ζ potential data of Bi_2Te_3 NPs synthesised with varying TOP concentrations in ethanol at 27 oC before and after ligand removal processes are displayed in Figures 5a and c, respectively. For BTt1, BTt2, BTt3, and BTt4, the average potentials and mobility following ligand removal under an applied electric field of 85 mV are 32.5, 16.5, 13.8, and 6.2 mV and 6.52x10-5, 3.31x10-5, 2.77x10-5, and 1.24x10-5 cm2/Vs, respectively (Figure 5a).

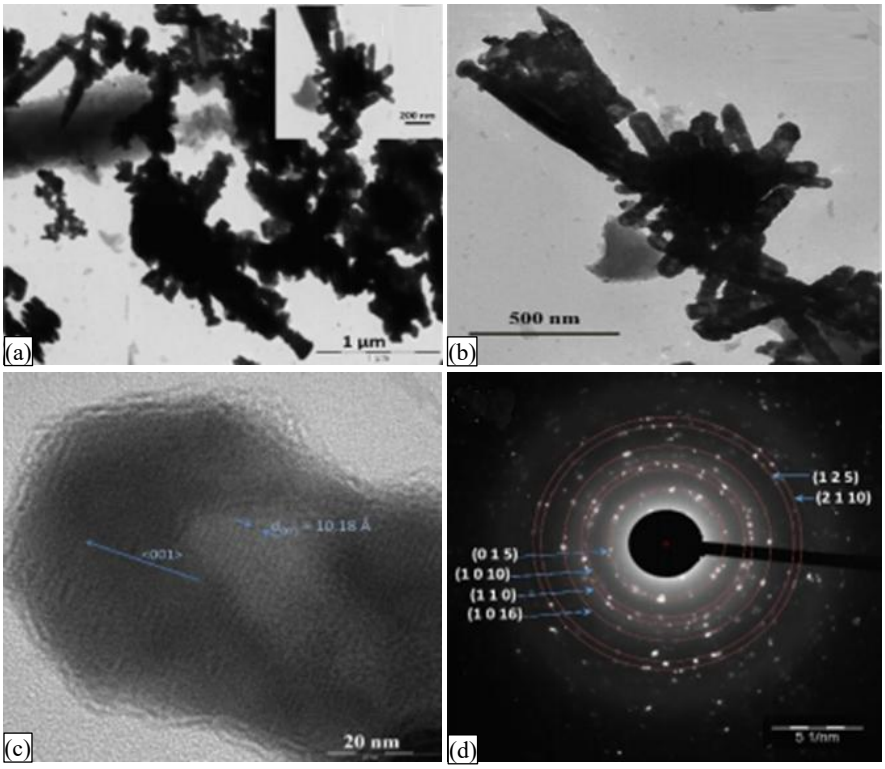

Figure 4. TEM pictures taken at various magnifications (a–b), high resolution TEM (c), and (d) chosen region electron diffraction of BTt4.

© STM Journals 2026. All Rights Reserved

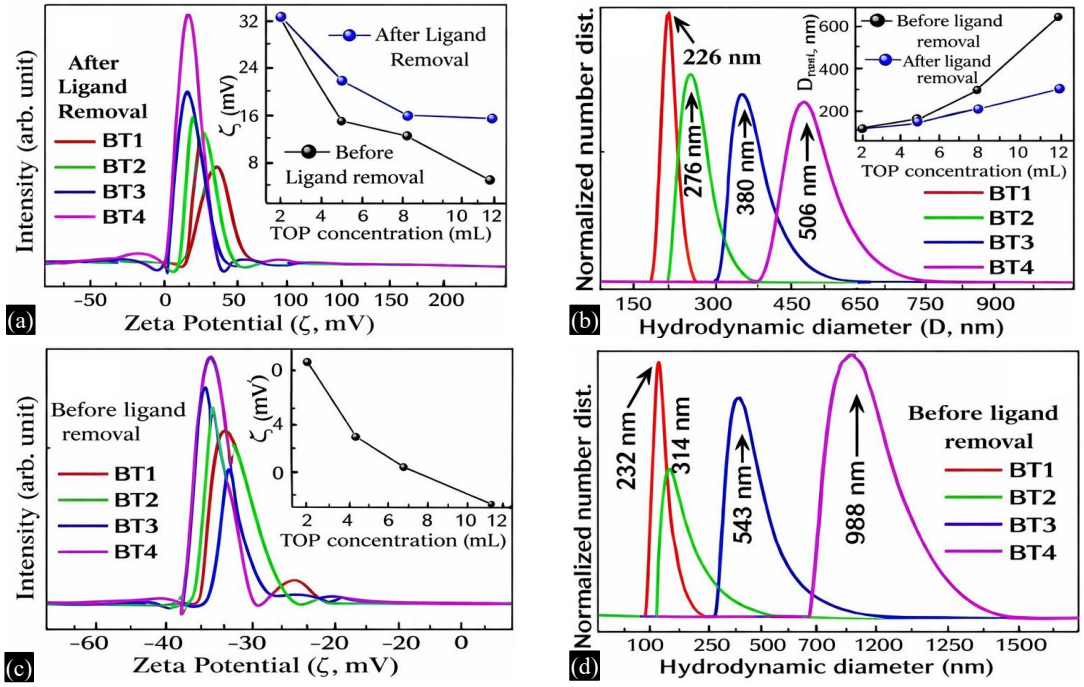

Figure 5 (a, c) Zeta potential and (b, d) hydrodynamic diameter of Bi_2Te_3 nanorods in ethanol at 27℃ after and before ligand removal steps, respectively, prepared in different TOP concentrations.

The ζ potential is really directly proportional to mobility, which is higher for smaller particles and is governed by the surface charge of charged NPs in colloidal solution [16, 33]. These samples similarly show similar tendencies with reduced ζ potential (or mobility) values prior to ligand removal (Figure 5c). The inset of Figure 5a illustrates how the ζ values change as TOP increases. The decrease in NPs' mobility or ζ potential is most likely the result of their colloidal size increasing. The thickness of the adsorption hydrocarbon layer on the surface of NPs, which might rise with TOP concentration, is included in the colloidal size. This improvement in the ζ potential magnitude for samples following ligand removal compared to the identical samples prior to ligand removal (inset of Figure 5a) suggests that the removal procedures remove some, if not all, of the hydrocarbons from the surface of NRs. In this case, only BTt1 (2 mL TOP) shows more than 30 mV following ligand removal, whereas the others show smaller ζ, suggesting that they are unstable in ethanol [16, 33].

Spectroscopic Studies

Ray Photoelectron Spectroscopy

A highly surface-sensitive method for better understanding the valence states of constituent elements, X-ray photoelectron spectroscopy (XPS) barely reaches a few nanometres into materials. Figure 6a displays the whole scale scan spectrum of the Bi_2Te_3 NPs as generated using the polyol technique (BTp). Shirley background is used in XPSPEAK41 program to match high resolution XPS spectra obtained for C 1s, Bi 4f, Te 3d, and O 1s with a Gaussian-Lorentzian mixture (Figure 6 b-e). As a point of reference, the carbon 1s peak (Figure 6b) can be de-convoluted into three peaks, which correspond to C-C or C=C, C-OH, and C=O [5], respectively, and are centered at 284.6 eV, 286.2 eV, and 288 eV. Figure 6c shows the two pairs of de-convoluted Bi 4f7/2 and 4f5/2 peaks. The first pair of peaks, centered at 157.2 eV and 162.5 eV, correspond to 4f7/2 and 4f5/2 of Bi3+ in Bi_2Te_3 [34.35], whereas the higher energy side peaks at 158.78 eV and 164.2 eV are of Bi3+ in Bi2O3/Bi(OH)3 [34]. The Te 3d high-resolution spectrum (Figure 6d) shows two pairs of peaks or four unique peaks. TeO2 or its hydroxide that is formed at the surface is reflected by the second pair of peaks, which are centered at 575.78 eV and 586.23 eV. The first pair of peaks, which are centered at 571.93 eV and 582.31 eV, are in good agreement with the binding energies of Te 3d5/2 and Te 3d3/2 of Bi_2Te_3 [34], respectively. Moreover, the O 1s peak can be de-convoluted into two peaks.

© STM Journals 2026. All Rights Reserved

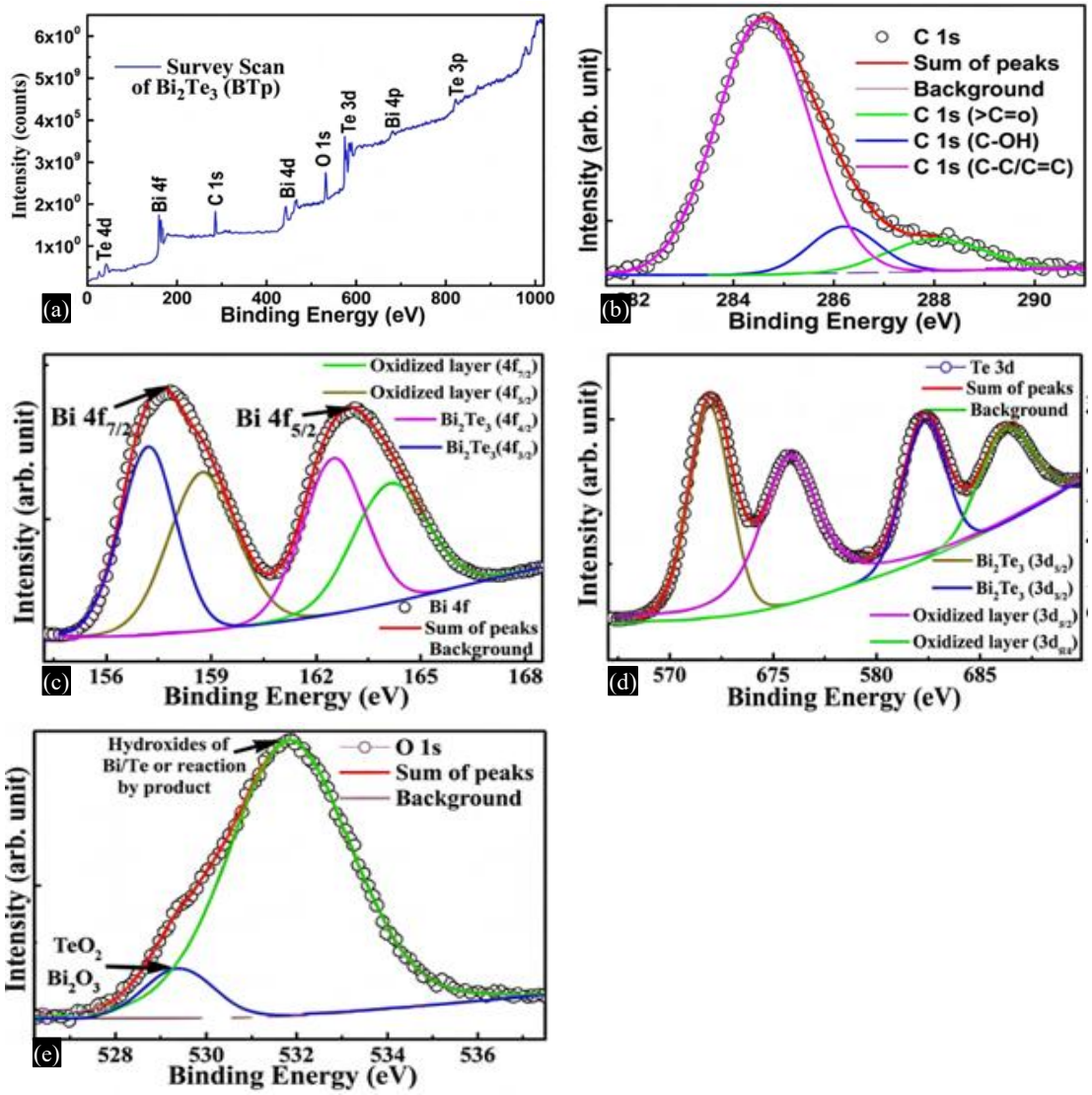

Figure 6. (a) Bi_2Te_3 (BTp) survey XPS spectral scan. high resolution XPS spectra of BTp with fitted curves for (b) C 1s, (c) Bi 4f, (d) Te 3d, and (e) O1s. Solid (red) curves represent the aggregate of all individual peaks, while open circles represent the raw data.

Adsorbed hydroxides of Bi or Te [35,36] and reaction by-products (C–O/C=O groups) [5] are responsible for the second notable peak at 531.86 eV, whereas the first low intensity peak, centred at 529.4 eV, is caused by O 1s of TeO2/Bi2O3 [34,36]. Bi2(Te,Se)3 systems frequently exhibit the observation of Bi/Te oxide peaks [34,36]. Because of Te/Se's high reactivity with oxygen atoms and moistures, Thomas et al. [36] observed that the oxidation of these systems followed logarithmic growth and reached saturation at around two weeks. Surfactants [10] and other materials [19] can be used to prevent this rapid oxidation of NPs. In order to control the size of the Bi_2Te_3 NPs and prevent surface oxidation, we employed TOP and OA.

CONCLUSIONS

Several approaches have been used to characterize the Bi_2Te_3 nanorods that were successfully synthesized utilizing the thermal decomposition method, and their thermoelectric properties have been examined. The conversion of single phase Bi_2Te_3 into BiTe-Bi_2Te_3 nanocomposites with increasing TOP concentration was verified by their Rietveld refinement. The stoichiometric production of Bi_2Te_3 is revealed by Raman spectra analysis, which also supports a regular decrease in crystallite size found

© STM Journals 2026. All Rights Reserved

in XRD. For the first time, Bi_2Te_3 nanorods' inversion symmetry is broken by ligands. FTIR is used to investigate if ligands are present on the surface of as-synthesized NPs. Utilizing XRD, TEM, FESEM, and DLS, the development of particle size with TOP concentration was examined. The production of ligand-capped Bi_2Te_3 with varying thicknesses is compatible with zeta potential measurements. Together with electrical resistivity and Hall measurements, the thermopower analysis verified that these nanocomposites are n-type semiconductors. Lastly, the 40 nm crystallite size Bi_2Te_3-BiTe nanocomposite exhibits the highest power factor. The general conclusion of this study will be briefly presented in the following chapter.

REFERENCES

1. F. J. DiSalvo, Science 285, 703 (1999).
2. B. Poudel, Q. Hao, Y. Ma, Y. C. Lan, A. Minnich, B. Yu, X. A. Yan, D. Z. Wang, A. Muto, D. Vashaee, et al. Science 320, 634 (2008).
3. L. D. Hicks and M. S. Dresselhaus, Phys. Rev. B 47, 12727 (1993).
4. S. V. Faleev and F. Leonard, Phys. Rev. B 77, 214304 (2008).
5. Tarachand, S. Hussain, N. P. Lalla, Y.-K. Kuo, A. Lakhani, V. G. Sathe, U. Deshpande and G. S. Okram, Phys.Chem.Chem.Phys. 20, 5926 (2018).
6. X. Shi, J. Yang, J. R. Salvador, M. Chi, J. Y. Cho, H. Wang, S. Bai, J. Yang, W. Zhangand L. Chen, Multiple-filled skutterudites: J. Am. Chem. Soc. 133, 7837 (2011).
7. Soni, Z. Yanyuan, Y. Ligen, M. K. K. Aik, M. S. Dresselhaus and Q. Xiong, Nano Lett. 12, 1203 (2012).
8. G. Zhang, B. Kirk, L. A. Jauregui, H. Yang, X. Xu, Y. P. Chen and Y. Wu, Nano Lett.12, 56 (2011).
9. S. Sumithra, N. J. Takas, D. K. Misra, W. M. Nolting, P. F. P. Poudeu and K. L. Stokes, Adv. Energy Mater. 1, 1141 (2011).
10. R. J. Mehta, Y. Zhang, C. Karthik, B. Singh, R. W. Siegel, T. Borca-Tasciuc, G. Ramanath, Nat. Mater. 11, 233 (2012).
11. M. Scheele, N. Oeschler, K. Meier, A. Kornowski, C. Klinke, and H. Weller, Adv.Funct. Mater. 19, 3476 (2009).
12. K. M. F. Shahil, M. Z. Hossain, V. Goyal and A. A. Balandin, J. Appl. Phys. 111, 1- 8 (2012).
13. M. Liu and X. Y. Qin, Appl. Phys. Lett. 101, 132103 (2012).
14. J. Martin, L. Wang, L. Chen, and G. S. Nolas, Phys. Rev. B 79, 115311 (2009).
15. S. Hwang, S.-I. Kim, K. Ahn, J. W. Roh, D.-J. Yang. S.-M. Lee and K.-H. Lee, J.Electronic Mater. 42, 1411 (2013).
16. Tarachand, V. Sharma, R. Bhatt, V. Ganesan and G. S. Okram, Nano Research 9, 3291 (2016).
17. Y. C. Dou, X. Y. Qin, D. Li, L. L. Li, T. H. Zou and Q. Q. Wang, J. Appl. Phys. 114, 044906 (2013).
18. J. Chen, T. Sun, D. H. Sim, H. Peng, H. Wang, S. Fan, H. H. Hng, J. Ma, F. Y. C.Boey, S. Li, et al., Chem. Mater. 22, 3086 (2010).
19. G. Yuan, Y. Li, N. Bao, J. Miao, C. Ge,Y. Wang, Mater. Chem. Phys. 143, 587 (2014).
20. Madavali, H. S. Kim, K. H. Lee, and S. J. Hong, J. Appl. Phys. 121, 225104 (2017).
21. W. J. Xie, X. F. Tang, Y. G. Yan, Q. J. Zhang, and T. M. Tritt, J. Appl. Phys. 105, 113713 (2009).
22. Purkayastha, F. Lupo, S. Kim, T. Borca-Tasciuc, and G. Ramanath, Adv. Mater.18, 496 (2006).
23. J. Singh, Tarachand, S. S. Samatham, D. Venkateshwarlu, Netram Kaurav, V. Ganesan and G. S. Okram, Appl. Phys. Lett. 111, 201904 (2017).
24. Tarachand, V. Sharma, J. Singh, C. Nayak, D. Bhattacharyya, N. Kaurav, S. N. Jha and G. S. Okram, J. Phys. Chem. C 120, 28354 (2016).
25. K. Wang, H.-W. Liang, W.-T. Yao, S.-H. Yu, J. Mater. Chem. 21, 15057 (2011).
26. Y. Zhao, J. S. Dyck, B. M. Hernandez, C. Burda, J. Phys. Chem. C 114, 11607 (2010).
27. Tarachand, M. Saxena, B. Mukherjee and G. S. Okram, Rev. Sci. Instrum. 90, 063904 (2019).
28. Soni and G. S. Okram, Rev. Sci. Instrum. 79, 125103 (2008).
29. S. Nakajima, J. Phys. Chem. Solids 24, 479 (1963).
30. Y. Feutelais, B. Legendre, N. Rodier, V. Agafonov, Mat. Res. Bull., 28, 591 (1993).

© STM Journals 2026. All Rights Reserved

31. M. Gharsallah, F. Serrano-Sánchez, J. Bermúdez, N. M. Nemes, J. L. Martínez, F. Elhalouani and J. A. Alonso, Nanoscale Res. Lett. 11, 142 (2016).
32. K. Momma and F. Izumi, J. Appl. Crystallogr. 44, 1272 (2011).
33. V. Delgado, F. G. Caballero, R. J. Hunter, L. K. Koopal, J. Lyklema, Interface Sci. 309, 194 (2007).
34. H. Bando, K. Koizumi, Y. Oikawa, K. Daikohara, V. A. Kulbachinskii and H. Ozaki, J. Phys.: Condens. Matter 12, 5607 (2000).
35. J. F. Moulder, W. F. Stickle, P. E. Sobol and K. D. Bomben, in Handbook of X-ray photoelectron spectroscopy, ed. J. Chastain, Perkin Elmer Corp., MN, 1992.
36. R. Thomas, M. K. Vallon, M. G. Frith, H. Sezen, S. K. Kushwaha, R. J. Cava, J. Schwartz and S. L. Bernasek, Chem. Mater. 28, 35 (2016).
37. K. M. F. Shahil, M. Z. Hossain, D. Teweldebrhan and A. A. Balandin, Appl. Phys. Lett. 96, 153103 (2010).
38. Y. J. Liang, W. Z. Wang, B. Q. Zeng, G. L. Zhang, Y. Y. Song, X. Y. Zhang, J. Huang, J. Li and T. Li, Solid State Commun. 151, 704 (2011).
39. F. Liu, L. Hu, M. Karakaya, P. Puneet, R. Rao, R. Podila, S. Bhattacharya, A. M. Rao, Scientific Reports 7, 16535 (2017).
40. Y. Zhao, R. W. Hughes, Z. Su, W. Zhou, D. H. Gregory, Angew. Chem. Int. Ed. 50, 10397 (2011).
41. P. Srivastava, K. Singh, J. Exp. Nanosci. 9, 1064 (2014).
42. M. Ibáñez, R. Zamani, S. Gorsse, J. Fan, S. Ortega, D. Cadavid, J. R. Morante, J. Arbiol, and A. Cabot, ACS Nano 7, 2573, (2013).
43. G. S. Okram, A. Soni, R. Rawat, Nanotechnology 19, 185711 (2008).
44. Z. H. Wang, L. Yang, X. J. Li, X. T. Zhao, H. L. Wang, Z. D. Zhang and X. P. A. Gao, Nano Lett. 14, 6510 (2014).
45. D.-H. Kim and T. Mitani, J. Alloys Com. 399, 14 (2005).
46. Y. Zhao, J. S. Dyck, B. M. Hernandez, C. Burda, J. Am. Chem. Soc. 132, 4982 (2010).
47. M. R. Dirmyer, J. Martin, G. S. Nolas, A. Sen, J. V. Badding, Small 5, 933 (2009).
48. S. Gupta, D. C. Agarwal, B. Sivaiah, S. Amrithpandian, K. Asokan, A. Dhar, B. K. Panigrahi, D. K. Avasthi, V. Gupta, Beilstein J. Nanotechnol. 10, 634-643 (2019).
49. V. Manzano, B. Abad, M. M. Rojo, Y. R. Koh, S. L. Hodson, A. M. L. Martinez,X. Xu, A. Shakouri, T. D. Sands, T. Borca-Tasciuc, M. Martin-Gonzalez, Scientific Reports 6, 19129 (2016).

© STM Journals 2026. All Rights Reserved